Photodoping through local charge carrier accumulation in alloyed hybrid perovskites for highly efficient luminescence

Sascha Feldmann [1,10], Stuart Macpherson [1,10], Satyaprasad P. Senanayak [1,2], Mojtaba Abdi-Jalebi [1], Jasmine P. H. Rivett[1], Guangjun Nan [3], Gregory D. Tainter [1], Tiarnan A. S. Doherty [1], Kyle Frohna [1], Emilie Ringe [4,5], Richard H. Friend [1], Henning Sirringhaus [1], Michael Saliba [6], David Beljonne[7], Samuel D. Stranks [1,8]* and Felix Deschler [1,9]*

Metal halide perovskites have emerged as exceptional semiconductors for optoelectronic applications. Substitution of the monovalent cations has advanced luminescence yields and device efficiencies. Here, we control the cation alloying to enhance optoelectronic performance through alteration of the charge carrier dynamics in mixed-halide perovskites. In contrast to single-halide perovskites, we find high luminescence yields for photoexcited carrier densities far below solar illumination conditions. Using time-resolved spectroscopy we show that the charge carrier recombination regime changes from second to first order within the first tens of nanoseconds after excitation. Supported by microscale mapping of the optical bandgap, electrically gated transport measurements and first-principles calculations, we demonstrate that spatially varying energetic disorder in the electronic states causes local charge accumulation, creating p- and n-type photodoped regions, which unearths a strategy for efficient light emission at low charge-injection in solar cells and light-emitting diodes.

M etal halide perovskites exhibit outstanding optoelectronic properties, such as low Urbach energies, high carrier mobilities and diffusion lengths, as well as very high photoluminescence quantum efficiencies (PLQEs)[1], which are essential to achieve performance limits in solar cells and light-emitting diodes (LEDs)[2–5]. This culminated in reported photovoltaic performances[6,7] exceeding 25% upon incorporation of a series of monovalent cation mixtures (formamidinium (FA), Cs) and passivating additives (Rb, K) to the methylammonium mixed-halide perovskite prototype[8,9] $MAPb(Br_{0.17}I_{0.83})_3$, as well as bright LEDs[10–15]. Here, we show that local bandgap variations in mixed-halide thin films yield photodoped regions for efficient photoluminescence (PL), favourable for optoelectronic applications.

Results

First, we find that external PLQEs for thin films of these configurations vary depending on composition, with values ranging from 2.7–40.9% champion performance from methylammonium lead bromide-iodide (MA) to potassium-passivated caesium methylammonium formamidinium lead bromide-iodide (KCsMAFA), respectively (Table 1), under solar illumination intensities and similar light outcoupling conditions (see Supplementary Fig. 1 for absorbance and PL spectra and Supplementary Fig. 2 for comparison of sample morphologies).

We investigate the charge carrier recombination processes underlying these observations with transient PL spectroscopy to resolve how cation composition affects carrier population dynamics (Fig. 1a). We find a large increase in lifetime of the PL kinetics upon incorporation of FA into $MAPb(Br_{0.17}I_{0.83})_3$ (yielding MAFA), shown in Fig. 1a (for other investigated compositions see Supplementary Table 1), indicating a decrease in non-radiative losses. Plotting the initial PL intensity (PL_0) against the initial excitation density (n_0) (Fig. 1a, inset) yields a quadratic dependence over a wide range of carrier densities, as expected for a bimolecular radiative recombination of electrons and holes[16].

We measure the dependence of PLQE on initial carrier density (Fig. 1b) and find that the values level out at high yield for low carrier densities. Considering a general recombination rate equation model of the form

$$-dn/dt_{tot} = an + bn^2 + cn^3 \qquad (1)$$

describing the total rate of change of carrier density (dn/dt_{tot}), where n is the carrier density, t is time and a, b and c are recombination constants[3], the internal PLQE ($PLQE_{int}$), given by the ratio of the radiative recombination rate (dn/dt_{rad}) to the total recombination rate

$$PLQE_{int} = \frac{dn/dt_{rad}}{dn/dt_{tot}} \qquad (2)$$

does not model the observed trends. The measured levelling out at low carrier densities is typical for doped semiconductors (see Supplementary Fig. 3), and we find our results are accurately

[1]Cavendish Laboratory, University of Cambridge, Cambridge, UK. [2]CSIR-Institute of Minerals & Materials Technology, Bhubaneswar, India. [3]Department of Physics, Zhejiang Normal University, Jinhua, China. [4]Department of Materials Science and Metallurgy, University of Cambridge, Cambridge, UK. [5]Department of Earth Sciences, University of Cambridge, Cambridge, UK. [6]Institute of Materials Science, Technische Universität Darmstadt, Darmstadt, Germany. [7]Chimie des Matériaux Nouveaux, Université de Mons, Mons, Belgium. [8]Department of Chemical Engineering & Biotechnology, University of Cambridge, Cambridge, UK. [9]Walter Schottky Institut, Physik Department, Technische Universität München, Garching, Germany. [10]These authors contributed equally: Sascha Feldmann, Stuart Macpherson. *e-mail: sds65@cam.ac.uk; felix.deschler@wsi.tum.de

described on the inclusion of a doping term p_D, when p describes the hole density, yielding equation (3) (see Methods for derivation):

$$\text{PLQE}_{int} = \frac{b(np + np_D)}{an + b(np + np_D)} \qquad (3)$$

The third-order Auger term was excluded as its contribution is negligible for the investigated carrier density regime. To shed light on the photoinduced doping effect in mixed-cation perovskite films, we track the total carrier population dynamics with broadband transient absorption (TA) spectroscopy and compare the ground-state-bleach kinetics with the PL kinetics in Fig. 1c (for TA spectra and kinetics see Supplementary Figs. 4 and 5, respectively). For the case of MA, both follow a similar decay at early times, before they eventually diverge at later times due to the bimolecular nature of PL recombination. By contrast, in MAFA (and all studied compositions containing FA), the PL does not follow the TA

Table 1 | Alloyed perovskite compositions investigated in this study

Abbreviation	External PLQE (%)	Composition
MA-I	16.8	$MAPbI_3$
MA	2.70	$MAPb(Br_{0.17}I_{0.83})_3$
MAFA	22.6	$MA_{0.2}FA_{0.8}Pb(Br_{0.17}I_{0.83})_3$
CsMAFA	21.6	$Cs_{0.05}(MA_{0.2}FA_{0.8})_{0.95}Pb(Br_{0.17}I_{0.83})_3$
RbCsMAFA	26.4	$Rb_{0.05}/Cs_{0.05}(MA_{0.2}FA_{0.8})_{0.95}Pb(Br_{0.17}I_{0.83})_3$
KCsMAFA	40.9	$K_{0.1}/Cs_{0.05}(MA_{0.2}FA_{0.8})_{0.95}Pb(Br_{0.17}I_{0.83})_3$

High external PLQEs were measured upon incorporation of a variety of monovalent cations and passivating additives to the mixed-halide prototype, using protocols reported in the literature[21,23,24]. Films were ~550 nm thick on glass substrates, measured at an excitation density of 10^{15} cm^{-3} (approximately solar illumination conditions).
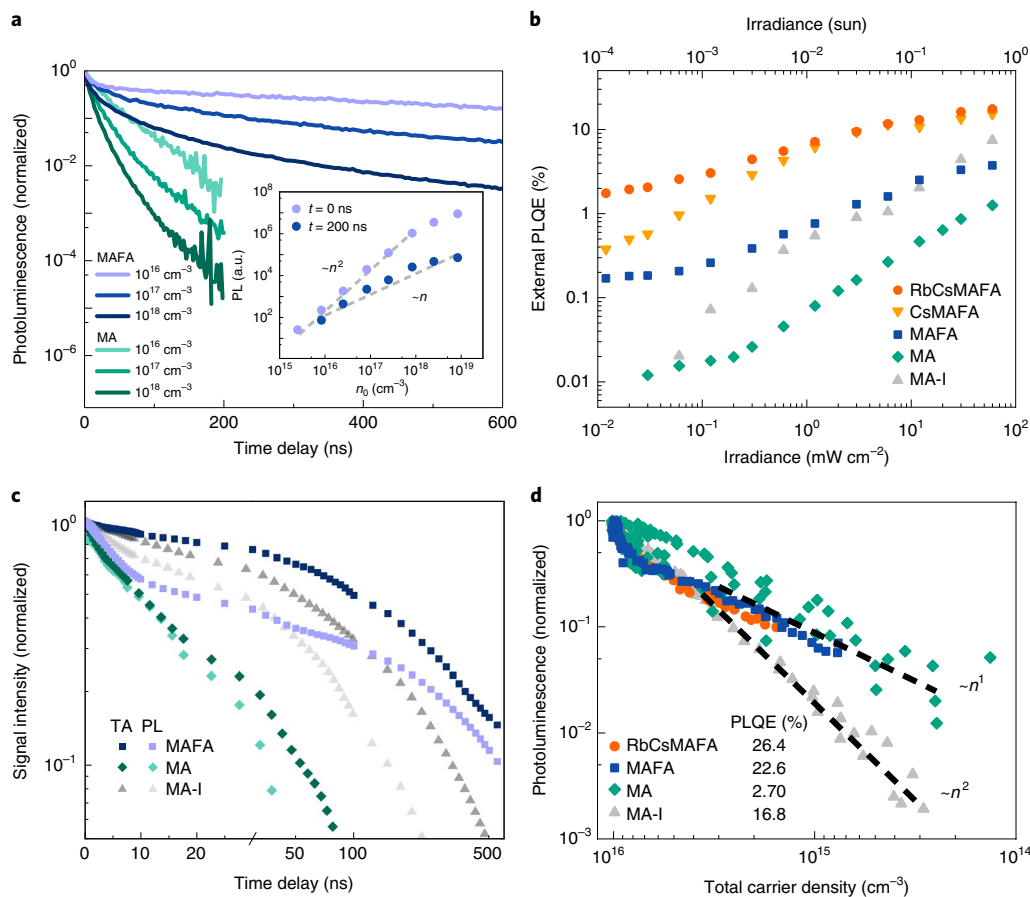

Fig. 1 | Charge carrier recombination dynamics. a, Transient PL kinetics of $MAPb(Br_{0.17}I_{0.83})_3$ (MA) and $MA_{0.2}FA_{0.8}Pb(Br_{0.17}I_{0.83})_3$ (MAFA) thin films with varying initial carrier density n_0. Incorporation of FA cations leads to a significant increase in PL lifetime (36 ± 1 ns for MA and 695 ± 69 ns for MAFA at $n_0 = 10^{16}$ cm^{-3}, respectively). Inset: PL intensity as a function of initial carrier density for MAFA. Initially, PL scales quadratically with carrier density (n^2) over a wide range of carrier densities, whereas at later times it scales linearly (n). **b**, Fluence-dependent external PLQE measurements. PLQE values level out at low excitation densities for mixed-halide compositions, in line with a doping carrier density of ~10^{14} cm^{-3}, while for MA-I the PLQE rapidly decreases. **c**, Tracking carrier recombination mechanisms with TA and PL kinetics at an initial carrier density of $n_0 = 10^{16}$ cm^{-3}, where TA quantifies the total carrier density and PL only the radiative fraction. In the first 10 ns after excitation, a drop occurs in PL in the case of MAFA films that is not present in TA. **d**, Dependence of PL intensity on total carrier density. For this, the time-dependence of the PL kinetics was transformed into a carrier-density-dependence using the total carrier density that was derived from TA measurements by setting time as an implicit variable. While MA-I shows a quadratic PL-dependence[3] on carrier density, first-order recombination behaviour is observed in compositions with mixed halides, resulting in high brightness at low carrier densities. We note that the highly efficient PL of MAFA and RbCsMAFA decayed too slowly to be mapped over carrier densities as low as for the faster decaying MA-I (due to second-order dependence) or MA (due to more non-radiative losses). See Supplementary Fig. 8 for CsMAFA and KCsMAFA PL kinetics.
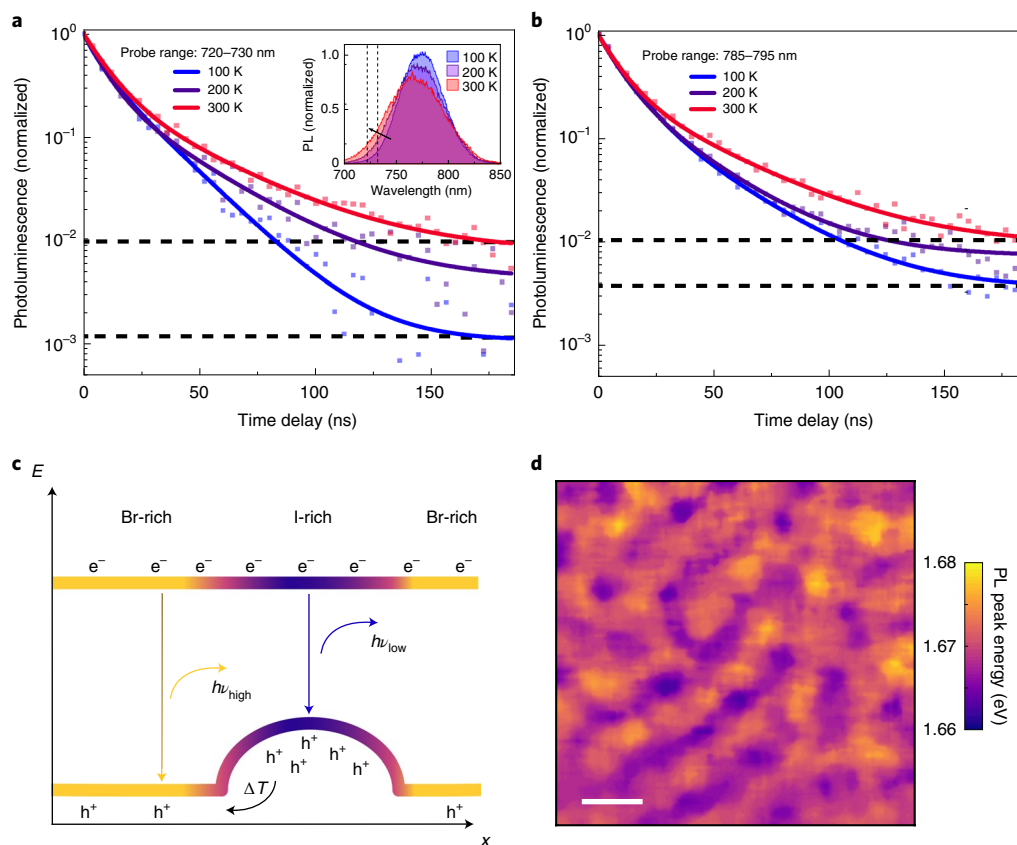
Fig. 2 | Temperature-dependent luminescence of mixed-halide MAFA films. a,b, PL kinetics, spectrally integrated over high-energy region, 720–730 nm (**a**), and low-energy region, 785–795 nm (**b**). At 300 K, both sides of the PL spectrum show similar kinetics, whereas at 100 K the high-energy part decays faster than its low-energy counterpart (indicated by black dotted lines as a guide to the eye). Inset in **a**: area-normalized temperature-dependent PL spectra. The arrow indicates a fourfold increase in integrated PL over 720–730 nm (dotted lines). The measurements were performed at an initial carrier density of $n_0 = 10^{16}\,cm^{-3}$. **c**, Schematic illustration of energetic disorder in the energy levels of mixed-cation perovskite films, where E is energy and x is space, providing a model for the dependence of high- and low-energy emission ($h\nu_{high}$ and $h\nu_{low}$, respectively) on temperature (T). This leads to spatial accumulation of one carrier type, invoking strong local doping. Thereby, radiative charge carrier recombination is diffusion-limited by the more mobile carrier type, and monomolecular. e⁻, electron; h⁺, hole. **d**, Confocal microscopy PL mapping of different domains in an MAFA mixed-halide film. The region-dependent PL peak energy difference is on the same order of magnitude as the measured activation energy, as described in the main text (see Supplementary Fig. 10). Scale bar, 5 µm.

signal initially. Instead, there is an initial drop in PL signal within 10 ns after photoexcitation, which indicates a decrease in radiative recombination rate, followed by a plateauing of PL intensity (see also Supplementary Fig. 6). The total carrier density in the material, reflected by TA, remains high. Still, much higher PLQE is observed in these films than in MA, suggesting an overall reduction in the impact of non-radiative recombination (Supplementary Fig. 7).

In Fig. 1d we first confirm for MAPbI₃ (MA-I) the reported second-order dependence[3] of PL on total carrier density (n_{total}), the latter being extracted from our TA kinetics using time as an implicit variable. Surprisingly, the addition of a small fraction of bromide anions in MA films leads to a change from second- to first-order dependence of PL on total carrier density. While the introduction of mixed halides in MA samples does change the recombination mechanism from bimolecular to monomolecular, the corresponding PLQE remains low. This indicates strong non-radiative losses due to higher defect densities than for MA-I, explaining why an initial drop in PL, similar to MAFA in Fig. 1c, cannot be resolved. However, the PLQE increases on addition of FA and for these MAFA mixed-halide films, the PL signal decays proportional to n, after an initial phase linked to the observed drop in PL within 10 ns, while for MA-I PL decays with n^2. This leads to the relative PL intensity of MAFA remaining approximately ten times higher than

for MA-I under low carrier densities comparable to solar illumination conditions (carrier density $\sim 10^{15}\,cm^{-3}$). The reasons discussed in the literature for the better performance of FA-containing films include suppressed ion migration compared with MA-only[17] and increased crystallinity through reduction of defect states in the bulk for MAFA[18–20]. FA cations stabilize the unexpected, beneficial change to first-order dependence of PL introduced by the mixed halides, to ultimately harvest this photodoping effect for high PLQEs. Adding Cs, Rb or K cations to the alloy continues to reduce non-radiative losses. The reported origins of these reduced losses include the reduction of defect states in the bulk lattice for Cs (refs. [21,22]) and Rb (refs. [22,23]), as well as surface passivation for K (ref. [24]), or stabilization of the crystal structure against lattice strain, also reducing non-radiative losses[25]—without changing the underlying recombination mechanism that remains effectively first order for all mixed-halide films.

We stress that this quasi-first-order dependence should not be confused with the first-order non-radiative rate constant in the overall evolution of carrier population, given by equation (1). Based on this equation, the recombination rate is dominated by the first-order non-radiative term at carrier densities low enough for the majority of charges to be trapped by defects (surface and bulk), yielding $-dn/dt \approx an$. Low carrier densities thus decay dominantly
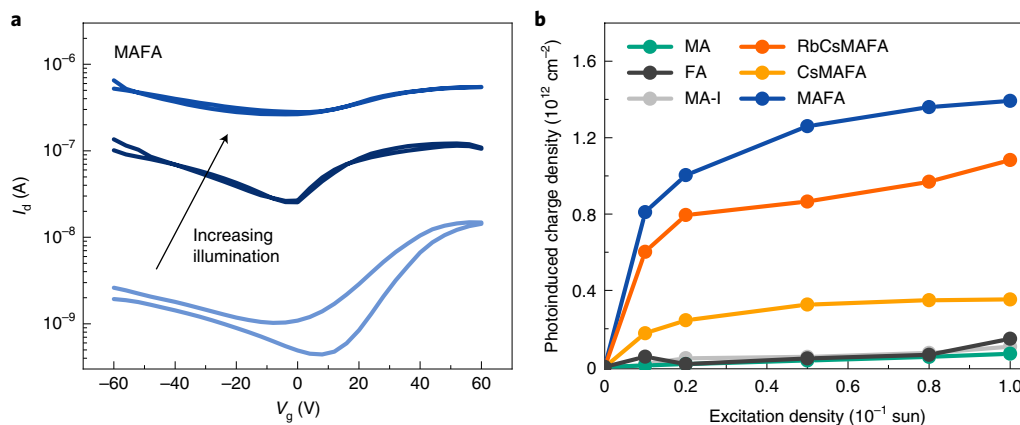
Fig. 3 | Electrically gated measurements on charge transport and photoinduced doping in mixed-cation perovskites. a, Exemplary transfer characteristics of an MAFA FET ($L = 100\,\mu m$, $W = 1\,mm$) for different excitation densities ranging between dark, 0.05 and 0.1 sun (white-light illumination), showing the drain current (I_d) as a function of gate voltage (V_g). **b**, Photoinduced charge density in perovskite thin-film FETs as a function of excitation density. Only in the presence of both MA and FA cations is a substantial increase in photoinduced charge density observed.

with $n(t) = n_0 e^{-at}$, while PL kinetics in this regime are described by $PL(t) \sim bn^2 = bn_0^2 \times e^{-2at}$. The PL will show a monoexponential decay, while the underlying recombination mechanism remains bimolecular and depends quadratically on the carrier density. In Fig. 1c we plot the kinetics of PL intensity and TA ground-state-bleach intensity, which is a measure for $n(t)$, and we find that at low carrier densities the PL of MA-I decays by a factor 2 faster than the TA signal, as expected from the above formulism. The combination of both TA and PL experiments is essential to provide detailed insights into the recombination mechanism, which is not possible from PL kinetics alone.

The origin of the first-order recombination and photodoping implied by the fluence-dependent PLQE experiments can arise from one charge carrier type accumulating locally in large excess due to heterogeneity in the energy landscape, creating n-/p-type regions of the film. To test the above hypothesis, we perform temperature-dependent and spatially resolved PL measurements (Fig. 2). We find that the PL of MAFA overall increases and that the peak redshifts with decreasing temperature (Supplementary Fig. 9), in line with earlier observations on related perovskite compounds[26]. The improved phase stability of FA-based mixed-halide compositions[27,28] enables us to compare the kinetics of the low-energy and high-energy regions of the PL spectrum at different temperatures (Fig. 2a,b). We find comparable kinetics in the low-energy region, but a drop in PL intensity for lower temperatures in the high-energy region—an observation that is highly unlikely to be explained by phonon interactions, since phonon absorption is much less likely than phonon emission, which we do not observe[29]. Thus, high-energy sites quickly become less populated at lower temperatures. These results strongly point towards energetic disorder in the film, which will localize charges in regions of local energy minima (Fig. 2c). Accumulation of electrons or holes in different regions of the film will then create local excess of one carrier species, with an energy barrier hindering them from returning to high-energy sites. The emission rate in these regions only depends on the density of minority carriers (the opposite charge density being dominated by the doping-induced density)—hence we observe first-order recombination. We note that these findings are different from reports on shallow traps[30,31], since such traps would ultimately result in increased fractions of non-radiative recombination and thus not lead to the observed increase in PL performance.

The PL peak energy map displayed in Fig. 2d confirms these different energy sites and shows a heterogeneous distribution of

local domains. We estimate the carrier transport length to these sites (L), using a diffusion-like model $L = \sqrt{D\Delta t}$ by considering reported diffusion constants ($D = 1.09\,cm^{-2}\,s^{-1}$ for MAFA)[32,33] and the timescale, Δt, of the initial PL drop in Fig. 1 (approximately 10 ns for MAFA)—the time taken for carriers to localize in low-energy regions and display first-order PL kinetics. Transport lengths on the order of $\sim 1.0 \pm 0.5\,\mu m$ are in accordance with domain sizes in the PL map (Fig. 2d). Further, the PL peak energy difference between different spatial regions is on the order of tens of millielectronvolts, matching activation energies for carriers found from an Arrhenius-like plot for the temperature-activated PL lifetime (Supplementary Fig. 10).

While typical grain sizes are on the order of few hundred nanometres (for example $\sim 200\,nm$ for MAFA, Supplementary Fig. 2), typical PL energy domain sizes cover several micrometres (for example ~ 2–$5\,\mu m$ for MAFA). This provides further evidence that sample morphology alone cannot be the origin of our observed photodoping. MA-I, with a very similar scanning electron microscopy profile does not show the same PL energy variation (Supplementary Fig. 11), providing strong evidence that the variation of iodide and bromide content is key. Compositional mapping using electron probe microanalysis (EPMA) shows I-rich and Br-rich regions with similar size as in our PL maps. This suggests the compositional heterogeneity is a consequence of an initial chemical distribution upon film formation, rather than light-induced halide segregation, which is common for less stable mixed-halide films than used here (Supplementary Fig. 12)[17,34,35].

Our observation that the increased PL yields arise from localized charge carrier accumulation has significance for the efficiency of both solar cells and LEDs. The observed charge accumulation regions are on the micrometre scale, laterally; with film thicknesses <1 μm it is likely that channels of the low-bandgap composition are present between the top and bottom surfaces, in which photoexcited carrier densities remain high, above the trap-limited regime. This leads to the desired scenario of dominant radiative recombination at device-relevant (that is, low) carrier densities. In LEDs, these channels are likely to act as efficient emitter regions for high PL efficiency at low carrier injection, while in solar cells they are a pathway of improved transport, reduced non-radiative losses and improved photon recycling[2] for efficient charge extraction and high open-circuit voltage in low-light conditions[36]. For these reasons, charge carrier doping has been important for a wide range of breakthroughs in current commercial semiconductor systems, such as GaAs, which
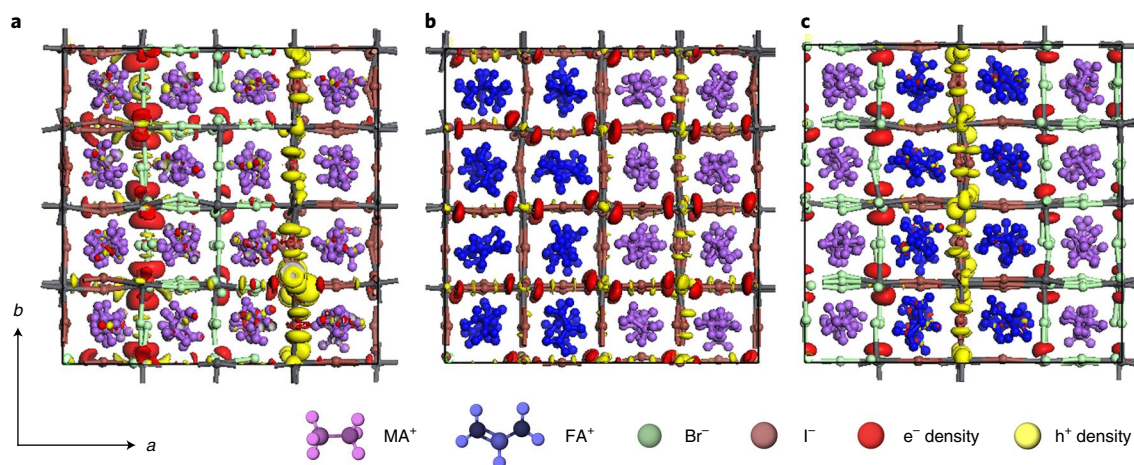
Fig. 4 | DFT and TDDFT calculations reveal driving force for mixed-halide mediated charge separation. a, Charge densities of the lowest excited-state geometry relaxed from the optimized ground-state geometry of the MAPbI$_3$/MAPbBr$_3$ heterojunction along the *a* axis, showing charge localization across the Br/I heterojunction. **b**, Charge densities of the lowest excited-state geometry relaxed from the optimized ground-state geometry of the FAPbI$_3$/MAPbI$_3$ heterojunction along the *a* axis, displaying no additional driving force for charge segregation across the MA/FA interface. **c**, Charge densities of the lowest excited state for the optimized ground-state geometry of the MAPbBr$_3$/FAPbI$_3$ heterojunction. The ground-state energy is 28.3 meV nm^{-3} smaller than the one for the MAPbI$_3$/FAPbBr$_3$ heterojunction (shown in the Supplementary Information), indicating matched ion radii stabilize charge separation across the lattice. The electron (hole) density is shown in red (yellow) in **a**–**c**; the value of the isosurface is 1.5 × 10^{-3} e Å^{-3} in **a** and **c**, and 7.0 × 10^{-4} e Å^{-3} in **b**. See Supplementary Fig. 14 for density of states (DOS) and charge densities of alternative geometries, Supplementary Fig. 15 for ground-state heterojunctions and Supplementary Fig. 16 for lowest excited-state charge densities for alternative configurations.

is a leading photovoltaic technology, with performance approaching the radiative limit[10,24,37]. We now find that charge carrier doping occurs intrinsically under illumination in the crudely processed perovskite thin-film semiconductors.

We probe the nature of the localized charge carriers and the extent of photodoping with field-effect transistor (FET) measurements on bottom-gate bottom-contact FETs (details in the Methods and the Supplementary Information) in the dark and under illumination, as set out in Fig. 3. The transfer characteristics (Fig. 3a and Supplementary Fig. 13) measured at room temperature in the dark and under illumination show loss of gate modulation at negative voltages, thereby confirming localization of holes, indicating excess localized p-type carriers, while electrons remain mobile and cannot be fully depleted. A strong increase in photoinduced carrier density, extracted from the capacitance, threshold voltage and maximum gate voltage, is observed for films containing FA cations (Fig. 3b). We take this as further validation of our spectroscopic observation that MA and FA ions must be present together to stabilize doping of higher carrier concentration in the mixed-halide perovskites. Potentially, FA ions facilitate a larger phase separation between bromide and iodide regions to allow for more stable charge accumulation or passivate the interface between these regions to reduce losses when carriers cross between them.

Finally, we perform density functional theory (DFT) and time-dependent DFT (TDDFT) calculations to model the Br/I and the MA/FA heterojunction in mixed-halide films, respectively (Fig. 4). These reveal a driving force for confining holes in iodide-rich and electrons in bromide-rich domains, though we stress that charge carriers can still visit both regions, as seen in the excited-state density distributions (Fig. 4a). This observation is in line with previously reported energy offsets between bromide- and iodide-based perovskites[38,39]. The calculations further indicate that at the MA/FA heterojunction no intrinsic driving force for charge separation is induced (Fig. 4b), suggesting predominantly lattice stabilization rather than an electronic influence. Lastly, Fig. 4c shows that matching the smaller MA ion with bromide and the larger FA ion with iodide reduces the energy of the system by almost 30 meV nm^{-3}

while maintaining charge separation across the heterojunction as opposed to an ion radius mismatch.

Conclusions

Our results have profound implications for solar cells and LEDs, in which efficient luminescence at low carrier densities is required for high performance. Charge confinement and energy gradients in two-dimensional/three-dimensional perovskite LEDs have so far been exploited to boost radiative efficiency[12,40,41] but require complex device engineering. Here, we find that mixed-halide perovskites form self-organized bandgap gradients, leading to charge accumulation in local low-bandgap regions—an effect that is stabilized by a tailored selection of cations. Our observation of exceptionally high levels of PLQEs at excitation densities below solar flux demonstrates a novel strategy for scalable, high-efficiency LEDs. For this, transfer rates into the accumulation regions and localization potentials can be tailored by chemical post-deposition treatments[42], precise control over spatial halide patterns from scalable phase self-organization[43], evaporation[44] and lithography[45–47] on the microscale to drive radiative yields towards their fundamental limits. In contrast to previously reported irreversible trapping of carriers in deep trap-states, which has been argued to slow down non-radiative recombination[48], our observed photodoping leads to charge separation and accumulation within a disordered landscape of bandgaps. The observed increases in luminescence yields originate from radiative rates outcompeting non-radiative losses, since carrier densities remain locally high in these charge-accumulation regions. While decoupling of the detailed distribution of emission sites and the relative contributions of bulk and surface recombination is beyond the scope of the current study, future efficiency gains are expected from addressing these questions and controlling the effect to maximize performance in LEDs and solar cells.

In summary, we report a change from second- to first-order charge carrier recombination in mixed-cation perovskites due to localized, photodoped regions—moving perovskite materials closer to semiconductors such as GaAs or GaN, where doping unlocked their full potential for optoelectronic technologies[49–52]. Our findings

contribute to the understanding of the excellent performance of alloyed perovskite optoelectronics to date and, importantly, highlight the potential for perovskites to approach the performance of GaAs photovoltaics and optoelectronics.

Online content

Any methods, additional references, Nature Research reporting summaries, source data, extended data, supplementary information, acknowledgements, peer review information; details of author contributions and competing interests; and statements of data and code availability are available at https://doi.org/10.1038/s41566-019-0546-8.

References

1. Deschler, F. et al. High photoluminescence efficiency and optically pumped lasing in solution-processed mixed halide perovskite semiconductors. *J. Phys. Chem. Lett.* **5**, 1421–1426 (2014).
2. Pazos-Outón, L. M. et al. Photon recycling in lead iodide perovskite solar cells. *Science* **351**, 1430–1433 (2016).
3. Richter, J. M. et al. Enhancing photoluminescence yields in lead halide perovskites by photon recycling and light out-coupling. *Nat. Commun.* **7**, 13941 (2016).
4. Pazos-Outón, L. M., Xiao, T. P. & Yablonovitch, E. Fundamental efficiency limit of lead iodide perovskite solar cells. *J. Phys. Chem. Lett.* **9**, 1703–1711 (2018).
5. Stranks, S. D., Hoye, R. L. Z., Di, D., Friend, R. H. & Deschler, F. The physics of light emission in halide perovskite devices. *Adv. Mater.* 1803336 (2018).
6. *Best Research-Cell Efficiencies* (NREL, accessed 09 September 2019); https://www.nrel.gov/pv/assets/pdfs/best-research-cell-efficiencies.20190802.pdf
7. Yang, W. S. et al. High-performance photovoltaic perovskite layers fabricated through intramolecular exchange. *Science* **348**, 1234–1237 (2015).
8. Jacobsson, T. J. et al. Extending the compositional space of mixed lead halide perovskites by Cs, Rb, K, and Na doping. *J. Phys. Chem. C* **122**, 13548–13557 (2018).
9. Li, W. et al. Chemically diverse and multifunctional hybrid organic–inorganic perovskites. *Nat. Rev. Mater.* **2**, 16099 (2017).
10. Braly, I. L. et al. Hybrid perovskite films approaching the radiative limit with over 90% photoluminescence quantum efficiency. *Nat. Photon.* **12**, 355–361 (2018).
11. Xiao, Z. et al. Efficient perovskite light-emitting diodes featuring nanometre-sized crystallites. *Nat. Photon.* **11**, 108–115 (2017).
12. Yuan, M. et al. Perovskite energy funnels for efficient light-emitting diodes. *Nat. Nanotechnol.* **11**, 872–877 (2016).
13. Gong, X. et al. Electron–phonon interaction in efficient perovskite blue emitters. *Nat. Mater.* **17**, 550–556 (2018).
14. Liu, Y. et al. Efficient blue light-emitting diodes based on quantum-confined bromide perovskite nanostructures. *Nat. Photon.* **13**, 760–764 (2019).
15. Tan, Z.-K. et al. Bright light-emitting diodes based on organometal halide perovskite. *Nat. Nanotechnol.* **9**, 687–692 (2014).
16. Davies, C. L. et al. Bimolecular recombination in methylammonium lead triiodide perovskite is an inverse absorption process. *Nat. Commun.* **9**, 293 (2018).
17. Hoke, E. T. et al. Reversible photo-induced trap formation in mixed-halide hybrid perovskites for photovoltaics. *Chem. Sci.* **6**, 613–617 (2015).
18. Salado, M., Calio, L., Berger, R., Kazim, S. & Ahmad, S. Influence of the mixed organic cation ratio in lead iodide based perovskite on the performance of solar cells. *Phys. Chem. Chem. Phys.* **18**, 27148–27157 (2016).
19. Pellet, N. et al. Mixed-organic-cation perovskite photovoltaics for enhanced solar-light harvesting. *Angew. Chem. Int. Ed.* **53**, 3151–3157 (2014).
20. Jesper Jacobsson, T. et al. Exploration of the compositional space for mixed lead halogen perovskites for high efficiency solar cells. *Energy Environ. Sci.* **9**, 1706–1724 (2016).
21. Saliba, M. et al. Cesium-containing triple cation perovskite solar cells: improved stability, reproducibility and high efficiency. *Energy Environ. Sci.* **9**, 1989–1997 (2016).
22. Solanki, A. et al. Cation influence on carrier dynamics in perovskite solar cells. *Nano Energy* **58**, 604–611 (2019).
23. Saliba, M. et al. Incorporation of rubidium cations into perovskite solar cells improves photovoltaic performance. *Science* **354**, 206–209 (2016).
24. Abdi-Jalebi, M. et al. Maximizing and stabilizing luminescence from halide perovskites with potassium passivation. *Nature* **555**, 497–501 (2018).
25. Jones, T. W. et al. Lattice strain causes non-radiative losses in halide perovskites. *Energy Environ. Sci.* **12**, 596–606 (2019).
26. Milot, R. L., Eperon, G. E., Snaith, H. J., Johnston, M. B. & Herz, L. M. Temperature-dependent charge-carrier dynamics in $CH_3NH_3PbI_3$ perovskite thin films. *Adv. Funct. Mater.* **25**, 6218–6227 (2015).
27. Galkowski, K. et al. Determination of the exciton binding energy and effective masses for methylammonium and formamidinium lead tri-halide perovskite semiconductors. *Energy Environ. Sci.* **9**, 962–970 (2016).
28. Tombe, S. et al. Optical and electronic properties of mixed halide (X = I, Cl, Br) methylammonium lead perovskite solar cells. *J. Mater. Chem. C* **5**, 1714–1723 (2017).
29. Wehrenfennig, C., Liu, M., Snaith, H. J., Johnston, M. B. & Herz, L. M. Homogeneous emission line broadening in the organo lead halide perovskite $CH_3NH_3PbI_{3-x}Cl_x$. *J. Phys. Chem. Lett.* **5**, 1300–1306 (2014).
30. Meggiolaro, D. et al. Iodine chemistry determines the defect tolerance of lead-halide perovskites. *Energy Environ. Sci.* **11**, 702–713 (2018).
31. De Angelis, F. & Petrozza, A. Clues from defect photochemistry. *Nat. Mater.* **17**, 383–384 (2018).
32. Herz, L. M. Charge-carrier mobilities in metal halide perovskites: fundamental mechanisms and limits. *ACS Energy Lett.* **2**, 1539–1548 (2017).
33. Hu, Y. et al. Understanding the role of cesium and rubidium additives in perovskite solar cells: trap states, charge transport, and recombination. *Adv. Energy Mater.* **8**, 1703057 (2018).
34. Sutter-Fella, C. M. et al. Cation-dependent light-induced halide demixing in hybrid organic-inorganic perovskites. *Nano Lett.* **18**, 3473–3480 (2018).
35. Zhang, H. et al. Phase segregation due to ion migration in all-inorganic mixed-halide perovskite nanocrystals. *Nat. Commun.* **10**, 1088 (2019).
36. Miller, O. D., Yablonovitch, E. & Kurtz, S. R. Strong internal and external luminescence as solar cells approach the Shockley–Queisser limit. *IEEE J. Photovoltaics* **2**, 303–311 (2012).
37. Spear, W. E. & Le Comber, P. G. Substitutional doping of amorphous silicon. *Solid State Commun.* **17**, 1193–1196 (1975).
38. Endres, J. et al. Valence and conduction band densities of states of metal halide perovskites: a combined experimental-theoretical study. *J. Phys. Chem. Lett.* **7**, 2722–2729 (2016).
39. Schulz, P. et al. Interface energetics in organo-metal halide perovskite-based photovoltaic cells. *Energy Environ. Sci.* **7**, 1377–1381 (2014).
40. Cho, H. et al. Overcoming the electroluminescence efficiency limitations of perovskite light-emitting diodes. *Science* **350**, 1222–1225 (2015).
41. Yang, X. et al. Efficient green light-emitting diodes based on quasi-two-dimensional composition and phase engineered perovskite with surface passivation. *Nat. Commun.* **9**, 570 (2018).
42. Cardenas-Daw, C., Simon, T., Stolarczyk, J. K. & Feldmann, J. Migration of constituent protons in hybrid organic-inorganic perovskite triggers intrinsic doping. *J. Am. Chem. Soc.* **139**, 16462–16465 (2017).
43. Woodward, P. M. A chessboard at the nanoscale. *Nat. Mater.* **6**, 549–551 (2007).
44. Liu, M., Johnston, M. B. & Snaith, H. J. Efficient planar heterojunction perovskite solar cells by vapour deposition. *Nature* **501**, 395–398 (2013).
45. Palazon, F., Akkerman, Q. A., Prato, M. & Manna, L. X-ray lithography on perovskite nanocrystals films: from patterning with anion-exchange reactions to enhanced stability in air and water. *ACS Nano* **10**, 1224–1230 (2016).
46. Hörantner, M. T., Zhang, W., Saliba, M., Wojciechowski, K. & Snaith, H. J. Templated microstructural growth of perovskite thin films via colloidal monolayer lithography. *Energy Environ. Sci.* **8**, 2041–2047 (2015).
47. Pourdavoud, N. et al. Photonic nanostructures patterned by thermal nanoimprint directly into organo-metal halide perovskites. *Adv. Mater.* **29**, 1605003 (2017).
48. Stranks, S. D. et al. Recombination kinetics in organic-inorganic perovskites: excitons, free charge, and subgap states. *Phys. Rev. Appl.* **2**, 034007 (2014).
49. Blakemore, J. S. Semiconducting and other major properties of gallium arsenide. *J. Appl. Phys.* **53**, R123 (1982).
50. Zhang, S. B. & Northrup, J. E. Chemical potential dependence of defect formation energies in GaAs: application to Ga self-diffusion. *Phys. Rev. Lett.* **67**, 2339–2342 (1991).
51. Dingle, R., Störmer, H. L., Gossard, A. C. & Wiegmann, W. Electron mobilities in modulation-doped semiconductor heterojunction superlattices. *Appl. Phys. Lett.* **33**, 665–667 (1978).
52. Mimura, T., Hiyamizu, S., Fujii, T. & Nanbu, K. A new field-effect transistor with selectively doped GaAs/n-Al_xGa_{1-x}As heterojunctions. *Jpn. J. Appl. Phys.* **19**, L225–L227 (1980).

Methods

Film preparation. Lead compounds were purchased from Tokyo Chemical Industry. Organic cation salts were purchased from GreatCell Solar. Caesium iodide, potassium iodide and rubidium iodide were ordered from Alfa Aesar. All other materials were purchased from Sigma-Aldrich.

Precursor solutions for the mixed-halide samples were produced by first dissolving PbI_2 (1.1 M) and $PbBr_2$ (0.22 M) in a mixture of anhydrous DMF and DMSO (4:1 v:v). The following additional steps were carried out to produce the respective compositions. $MAPb(I_{0.83}Br_{0.17})_3$: add 1 M MAI and 0.2 M MABr; $MA_{0.17}FA_{0.83}Pb(I_{0.83}Br_{0.17})_3$ perovskite: add 1 M FAI and 0.2 M MABr; $Cs_{0.06}MA_{0.15}FA_{0.79}Pb(I_{0.84}Br_{0.16})_3$ perovskite: add 1 M FAI and 0.2 M MABr, dissolve 1.5 M CsI in DMSO, add CsI solution to precursor solution in 5% volume ratio (5:95 v:v); $Rb_{0.05}/Cs_{0.05}(MA_{0.15}FA_{0.79})_{0.95}Pb(I_{0.84}Br_{0.16})_3$ perovskite: as for CsMAFA, dissolve 1.5 M RbI in a mixture of DMF:DMSO 4:1 (v:v), add RbI solution to CsMAFA solution in 5% volume ratio (5:95 v:v); $K_{0.1}/Cs_{0.05}(MA_{0.15}FA_{0.79})_{0.95}Pb(I_{0.84}Br_{0.16})_3$ perovskite: as for CsMAFA, dissolve 1.5 M KI in a mixture of DMF:DMSO 4:1 (v:v), add KI solution to CsMAFA solution in 10% volume ratio (10:90 v:v). Bare perovskite films were spin-coated using a two-step procedure in a nitrogen atmosphere. Precursor solutions were deposited on glass cover slides and spun at 2,000 r.p.m. for 10 s, then 4,000 r.p.m. for 35 s. 150 μl of chlorobenzene was added 30 s after commencement of the procedure. Films were annealed at 100 °C for 1 h.

$MAPbI_3$ films were prepared based on the protocols of ref. [53]. Glass slides were coated with 60 μl of a 1.5 mg ml^{-1} solution of poly(bis(4-phenyl) (2,4,6-trimethylphenyl)amine) (PTAA) (M_w = 19,000 g mol^{-1}) in toluene (Sigma-Aldrich) using a two-step spin-coating procedure: 500 r.p.m. for 4 s, then 4,500 r.p.m. for 20 s. PTAA films were annealed at 70 °C for 10 min. MA-I precursor solutions were prepared by dissolving anhydrous 0.6 M $Pb(CH_3COO)_2$ (TCI), 0.067 M $PbCl_2$ (Sigma-Aldrich), 2 M MAI (Greatcell Solar) and 0.067 M DMSO (Sigma-Aldrich) in DMF (Sigma-Aldrich). The MA-I solution was heated to 75 °C during film deposition. 100 μl of solution was deposited and spun at 2,000 r.p.m. for 10 s, then 6,000 r.p.m. for 30 s. The films were annealed at 75 °C for 2 min then capped with a layer of poly(methyl methacrylate) (Aldrich, M_w = 996,000), 30 mg ml^{-1} in chlorobenzene (Sigma-Aldrich). 60 μl was deposited on the MA-I film and spun at 4,000 r.p.m. for 30 s before drying at 75 °C for 5 min.

Time-resolved photoluminescence spectroscopy. Time-resolved photoluminescence spectroscopy was recorded by a gated intensified charge-coupled device (iCCD) camera (Andor Star DH740 CCI-010) connected to a grating spectrometer (Andor SR303i). The pulsed output from a mode-locked Ti:sapphire optical amplifier (Spectra-Physics Solstice, 1.55 eV photon energy, 80 fs pulse width) was used to produce 400 nm excitation via second-harmonic generation in a β-barium borate crystal. The iCCD gate (width 5 ns) was stepped in 5 ns increments, relative to the pump pulse, to enable temporal resolution of the PL signal.

For temperature-dependent measurements, sample temperature was maintained in a cold finger cryostat, under vacuum. Constant liquid helium flow through the heat exchanger, and a temperature controller connected to a copper filament heater allowed for temperature regulation and stabilization.

Transient absorption spectroscopy. TA spectroscopy is a form of pump–probe spectroscopy that measures the variation in absorption by a sample, of a broadband probe spectrum, under photoexcitation by a pump source. By stepping the pump–probe delay, the carrier recombination kinetics of the sample can be investigated.

The second harmonic of a pulsed $Nd:YVO_4$ laser (AOT-YVO-25QSPX) was used as the pump beam (500 ps pulse width, 500 Hz repetition rate, 2.33 eV photon energy). The probe spectrum was generated using a home-built noncollinear optical parametric amplifier, pumped by the second harmonic of the same Ti:sapphire amplifier (Spectra-Physics Solstice). A delay generator was used to electronically vary the pump–probe delay. Transmitted probe and reference pulses were recorded with an n-type metal–oxide–semiconductor (NMOS) linear image sensor (Hamamatsu S8381-1024Q) and processed by a customized peripheral component interconnect (PCI) interface from Entwicklungsbüro Stresing.

Photoluminescence quantum efficiency. PLQE measurements were conducted to establish the ratio of radiative decay to non-radiative decay in photoexcited perovskite films. Excitation was provided by a continuous-wave diode laser (Thorlabs L520P50, 2.38 eV photon energy). As outlined in ref. [54], three measurements were made on each sample to establish the external PLQE at some excitation fluence. The samples were housed in an integrating sphere to collect all PL and any reflected or transmitted laser light, which was then fibre-coupled to a spectrometer (Andor iDus DU420A-BVF). Measurements were recorded with the laser directly on the sample, off the sample and with no sample present.

Rationale of doping term in PLQE. The model applied in the main text is based on extensive studies of classical inorganic semiconductors such as Si or GaAs, in which doping determines charge carrier recombination rates, initially based on work by Shockley, Read and Hall where the derivation of equation (3) can be found in more detail[55,56]. This was then applied to hybrid perovskites by our group, as well as the groups of Herz and Beard[3,5,16,57–60]. All these studies are based on

and give evidence for the model of a non-radiative monomolecular and radiative bimolecular recombination of free carriers that provide the physical background of our work. Starting from the general rate equation (equation (1)) and the relation of radiative to total recombination rates that describe the PLQE (equation (2)), but excluding the third-order Auger term (relevant only at higher carrier densities than considered in this study), leads to:

$$PLQE_{int} = \frac{dn/dt_{rad}}{dn/dt_{tot}} = \frac{bn^2}{an + bn^2} \quad (4)$$

If now the simple carrier density n is expanded to distinguish between electron (n) and hole (p) density, as well as a negative (n_D) and positive (p_D) doping density, equation (4) expands to

$$PLQE_{int} = \frac{dn/dt_{rad}}{dn/dt_{tot}} = \frac{b(n + n_D)(p + p_D)}{an + b(n + n_D)(p + p_D)} \quad (5)$$

With significant hole doping and insignificant electron doping as we observe in our work, we can assume the Shockley–Read–Hall recombination rate reduces to an, as it is limited by the minority electron density. With $p_D \gg n_D$ it follows:

$$PLQE_{int} = \frac{bn(p + p_D)}{an + b(np + np_D)} \quad (6)$$

which can be expanded to equation (3) in the main text.

Discussion of PL kinetics. In Fig. 1c and Supplementary Fig. 6 the PL kinetics of MAFA show an initial drop at early time that is not present in TA. The MA-I sample—due to the absence of mixed halides—does not show such an initial drop. The divergence at later times in MA-I can be explained by the fact that TA kinetics decay proportional to the carrier density $n(t)$, while PL kinetics decay proportional to n^2.

In MAFA, on the other hand, the PL signal undergoes an initial decrease followed by a plateauing that indicates the onset of the effective first-order radiative recombination due to a doping carrier density. The MAFA PL decay begins to track the TA signal (which directly maps out the carrier density) and does not diverge from it, indicating that the radiative recombination outcompetes non-radiative recombination due to photodoping, as is clear from the effective first-order dependence of PL on carrier density in Fig. 1d.

Confocal microscopy measurements. Photoluminescence measurements were acquired using a WITec alpha300 S set-up. The excitation source was a 405 nm continuous-wave laser (Coherent CUBE) with a fluence of 6 W cm^{-2}. The light was coupled though an optical fibre to the microscope and focused using a ×100 Nikon lens (NA = 0.95, spot size 1.5 μm). Samples rested on an X–Y piezo stage of the microscope. The PL signal was collected in reflection mode with the same ×100 objective and detected using a Princeton Instruments SP-2300i spectrometer fitted with an Andor iDus 401 CCD detector. A long-pass filter with a cut-off wavelength of 450 nm was implemented before signal collection to block the excitation. The PL peak energy was determined from the spectrum at each position using a centre-of-mass fit.

Electron probe microanalysis. EPMA was performed with a Cameca SX100 at the Earth Sciences Department, University of Cambridge. A 15 kV electron beam with a probe size of 1 μm was used with a current of 20 nA. I and Br were analysed on peak on large pentaerythritol (LPET) and large thallium acid phthalate (LTAP) crystals, respectively. Each pixel in the elemental maps was acquired with a 300 ms dwell time (longer dwell times were avoided to prevent sample damage), with a step size of 500 nm.

Transistor experiments. Bottom-gate bottom-contact perovskite FETs were fabricated using a Si/SiO_2 (300 nm) substrate on which Cr/Au source drain electrodes (25 nm) were lithographically patterned with a channel length of 100 μm and width of 1 mm. Perovskite thin films were spin-coated at 5,000 r.p.m. for 180 s using a standard antisolvent technique as used for the spectroscopic measurement to obtain films of thickness ~150 nm. The devices were then annealed for 30 min at 100 °C. All the devices were characterized in a vacuum chamber (10^{-6} mbar) using an Agilent 4155B parameter analyser, operated in pulsed mode. For the transfer measurement, the gate voltage (V_g) was applied over a short impulse of 0.5 ms and the transfer characteristics were measured. For the photoillumination study, the device was illuminated from the top with an intensity-controllable white-light source with a maximum intensity of 10 mW cm^{-2}. The interfacial charge density is given by the expression: $Q = C(V_{gmax} - V_{th})/e$, where C is the capacitance per unit area, V_{th} is the threshold voltage, V_{gmax} is the maximum gate voltage and e is the unit electronic charge. Photoinduced charge density is then estimated from the shift in V_{th} obtained by comparing the dark transfer characteristics with transfer characteristics obtained after illumination.

Computational details. The heterojunctions adopted in this work are based on cubic phases of $MAPbI_3$ (ref. [61]), $MAPbBr_3$ (ref. [61]), $FAPbI_3$ (ref. [62]) and $FAPbBr_3$

(ref. [63]). For the cubic $FAPbI_3$/$MAPbI_3$ heterojunctions, the lattice constant is 25.38 Å, which introduces a lattice mismatch of only −0.24% and +0.24% for $FAPbI_3$ and $MAPbI_3$, respectively. For the cubic $MAPbI_3$/$MAPbBr_3$ heterojunctions, the lattice constant is 24.46 Å, which yields a lattice mismatch of −3.4% and 3.6% for $MAPbI_3$ and $MAPbBr_3$, respectively. As far as the cubic $MAPbBr_3$/$FAPbI_3$ and $MAPbI_3$/$FAPbBr_3$ heterojunctions are concerned, the chosen constant (24.58 Å) is set up by averaging the lattice parameters of the $4 \times 4 \times 4$ supercells for $MAPbI_3$, $MAPbBr_3$, $FAPbI_3$ and $FAPbBr_3$, which then gives the lattice mismatch of −2.9%, 4.2%, −3.4% and 2.6%, respectively. Owing to the universal dynamics of organic cations in the metal halide perovskites[64], each of the heterojunctions has a paraelectric configuration with randomly oriented organic cations.

We optimize the ground-state geometries of these heterojunctions based on the DFT approach using the Vienna ab initio simulation package (VASP)[65] and employing the Perdew–Burke–Ernzerhof functional[66] in conjunction with the projector augmented-wave method[67]. The semi-empirical DFT-D2 method is used to account for the van der Waals corrections[68]. The cut-off energy used for the plane-wave basis set is 400 eV, and a k mesh with only the Γ point is used during the geometry relaxation that has been shown to reasonably predict the bandgap for the metal halide perovskites, with the sizes being comparable to the heterojunctions in this work[69]. The convergence criterions for total energies and forces are set to be 10^{-4} eV and 0.04 eV Å^{-1}, respectively. The electronic excitation and excited-state geometric relaxation are obtained by employing a recently developed TDDFT approach in the framework of linear response theory[70], which calculates the charge densities and ionic forces of large-scale systems in the excited states, by the derivatives of the Lagrangian functional with respect to external potential and ionic position, respectively.

Data availability
The data that support the plots within this paper and other findings of this study are available at the University of Cambridge Repository (https://doi.org/10.17863/CAM.43748).

References
53. Liu, Z. et al. Open-circuit voltages exceeding 1.26V in planar methylammonium lead iodide perovskite solar cells. *ACS Energy Lett.* **4**, 110–117 (2019).
54. De Mello, J. C., Wittmann, H. F. & Friend, R. H. An improved experimental determination of external photoluminescence quantum efficiency. *Adv. Mater.* **9**, 230–232 (1997).
55. Shockley, W. & Read, W. T. Statistics of the recombinations of holes and electrons. *Phys. Rev.* **87**, 835–842 (1952).
56. Hall, R. N. Electron-hole recombination in germanium. *Phys. Rev.* **87**, 387 (1952).
57. Liu, Y. et al. Temperature-dependent photoluminescence spectra and decay dynamics of $MAPbBr_3$ and $MAPbI_3$ thin films. *AIP Adv.* **8**, 95108 (2018).
58. Johnston, M. B. & Herz, L. M. Hybrid perovskites for photovoltaics: charge-carrier recombination, diffusion, and radiative efficiencies. *Acc. Chem. Res.* **49**, 146–154 (2016).
59. Yang, Y. et al. Low surface recombination velocity in solution-grown $CH_3NH_3PbBr_3$ perovskite single crystal. *Nat. Commun.* **6**, 7961 (2015).
60. Yang, Y. et al. Top and bottom surfaces limit carrier lifetime in lead iodide perovskite films. *Nat. Energy* **2**, 16207 (2017).
61. Poglitsch, A. & Weber, D. Dynamic disorder in methylammoniumtrihalogenoplumbates (II) observed by millimeter-wave spectroscopy. *J. Chem. Phys.* **87**, 6373 (1987).
62. Weller, M. T., Weber, O. J., Frost, J. M. & Walsh, A. Cubic perovskite structure of black formamidinium lead iodide, α-$[HC(NH_2)_2]PbI_3$, at 298K. *J. Phys. Chem. Lett.* **6**, 3209–3212 (2015).
63. Zhumekenov, A. A. et al. Formamidinium lead halide perovskite crystals with unprecedented long carrier dynamics and diffusion length. *ACS Energy Lett.* **1**, 32–37 (2016).
64. Fabini, D. H. et al. Universal dynamics of molecular reorientation in hybrid lead iodide perovskites. *J. Am. Chem. Soc.* **139**, 16875–16884 (2017).
65. Kresse, G. & Furthmuller, J. Efficient iterative schemes for ab initio total-energy calculations using a plane-wave basis set. *Phys. Rev. B* **54**, 11169 (1996).
66. Perdew, J. P., Burke, K. & Ernzerhof, M. Generalized gradient approximation made simple. *Phys. Rev. Lett.* **77**, 3865–3868 (1997).
67. Blochl, P. E. Projector augmented-wave method. *Phys. Rev. B* **50**, 17953 (1994).
68. Grimme, S. Semiempirical GGA-type density functional constructed with a long-range dispersion correction. *J. Comput. Chem.* **27**, 1787–1799 (2006).
69. Yin, W.-J., Shi, T. & Yan, Y. Superior photovoltaic properties of lead halide perovskites: insights from first-principles theory. *J. Phys. Chem. C* **119**, 5253–5264 (2015).
70. Zhang, X. & Lu, G. Subspace formulation of time-dependent density functional theory for large-scale calculations. *J. Chem. Phys.* **143**, 064110 (2015).

Author contributions
S.F., S.M., S.D.S. and F.D. conceived and planned the experiments with additional input from H.S., M.S., D.B. and R.H.F. J.P.H.R., S.M., M.A.-J. and K.F. fabricated the samples for spectroscopy measurements. S.F., S.M., J.P.H.R. and M.A.-J. performed the PLQE, TA and PL spectroscopy measurements. S.P.S. fabricated and measured the field-effect transistors with input from H.S. G.D.T. performed the confocal PL microscopy measurements. E.R., S.M. and T.A.S.D. prepared and performed EPMA measurements. G.N. and D.B. performed the DFT and TDDFT calculations. S.F. and F.D. drafted the manuscript and compiled figures, with discussion of results and feedback on the manuscript from all authors.

Competing interests
The authors declare the following competing financial interest: S.D.S. is a co-founder of Swift Solar Inc.

Additional information
Supplementary information is available for this paper at https://doi.org/10.1038/s41566-019-0546-8.

Correspondence and requests for materials should be addressed to S.D.S. or F.D.

Reprints and permissions information is available at www.nature.com/reprints.